Title

Divergent iron-regulatory states contribute to heterogeneity in breast cancer aggressiveness

Authors

William D. Leineweber[1], Ali Khalilimeybodi[2], Padmini Rangamani[2], Stephanie I. Fraley[1]*

Abstract

Similar primary tumors can progress to vastly different outcomes, where transcriptional state rather than mutational profile predicts prognosis. A key challenge is to understand how such programs are induced and maintained to enable metastasis. In breast cancer cells, aggressive transcriptional signatures and migratory behaviors linked to poor patient prognosis can emerge as a result of contact with a collagen-rich microenvironment mimicking tumor stroma. Here, we leverage heterogeneity in this response to identify the programs that sustain invasive behaviors. Invasive responders are characterized by expression of specific iron uptake and utilization machinery, anapleurotic TCA cycle genes, actin polymerization promoters, and Rho GTPase activity and contractility regulators. Non-invasive responders are defined by actin and iron sequestration modules along with glycolysis gene expression. These two programs are evident in patient tumors and predict divergent outcomes, largely on the basis of ACO1. A signaling model predicts interventions and their dependence on iron availability. Mechanistically, invasiveness is initiated by transient HO-1 expression that increases intracellular iron, mediating MRCK-dependent cytoskeletal activity and increasing reliance on mitochondrial ATP production rather than glycolysis.

Introduction:

Metastasis causes 60-90% of cancer deaths (1, 2), and many experts believe that targeting initial metastatic invasion and secondary spread will be the most effective strategy for reducing cancer mortality (2, 3). Despite this clinical impetus, there are few effective treatments that specifically target metastasis (4). This is in part because the genetic determinants of tumor initiation and early progression do not distinguish whether a tumor will metastasize (5–8). Instead, many cancers acquire metastatic capabilities by co-opting programs necessary for normal physiological processes (9–12). It is particularly unclear how cancer cells activate and sustain transcriptional programs that would normally be transient under physiological conditions to carry out metastatic functions. Accumulating evidence suggests that exposure to various microenvironmental factors

[1] Department of Bioengineering; University of California, San Diego, La Jolla, CA, 92093; United States
* sifraley@ucsd.edu
[2] Department of Mechanical and Aerospace Engineering; University of California, San Diego, La Jolla, CA, 92093; United States

could induce stable transcriptional responses that enable metastatic capabilities (13, 14). However, questions remain regarding why only a subset of cells exposed to such factors acquire the metastatic phenotype, and what features define the metastatic phenotype (15).

Recently, collective cell migration has emerged as a new paradigm for defining the metastatic phenotype (16). Aggressive solid tumors across multiple cancer types produce strands of collectively invasive tumor cells (17, 18) that have been linked to circulating tumor cell clusters and have greater metastatic potential than single cells (19). *In vitro* models of collective invasion induce this phenotype by embedding cells in dense extracellular matrices (ECMs) (20–22). Dense ECM is a hallmark of the tumor microenvironment (TME) and contributes both to tumorigenesis and metastasis, especially in breast cancer patients (23–26). Our prior work using bulk sequencing analysis has shown that cancer cells upregulate a transcriptional program that is predictive of poor prognosis when embedded in dense collagen prior to undergoing collective invasion, and this response is related to oxidative stress (21, 27). Here, we identify the mechanisms driving and sustaining collective invasion by leveraging the fact that not all breast cancer cells within a population respond in the same way. By conducting single cell sequencing analysis guided by phenotypic heterogeneity, we identify key determinants of response. We find that distinct responses arise from divergent states of iron regulation that link to Rho-GTPase, contractile machinery, and metabolism regulation. We show evidence for these states in human breast tumors and find that they are predictive of opposing clinical outcomes, driven largely by expression of the bi-functional iron sensor ACO1. Heme oxygenase I (HO-1), an iron-releasing enzyme, initiates the invasive state which is sustained by an "iron-addicted" transcriptional program. In HO-1 knockdowns, exogenous iron can rescue invasion. A model of the two state regulatory network predicts that in addition to iron, the glycolysis regulator enolase I (ENO1) controls phenotypic divergence, which we validate experimentally. This study defines a systems level model for the role that iron plays in breast cancer cell invasion and implicates specific biomarkers and therapeutic strategies for further investigation.

Results:

<u>Distinct modes of cytoskeletal regulation underlie breast cancer migration heterogeneity, with MRCK serving as a critical regulator of collective invasion.</u>

Breast cancer cells can be induced to undergo collective migration mimicking metastatic invasion by culturing them in high density collagen I (18, 21, 22). However, these experiments typically involve embedding multicellular cancer spheroids in collagen, such that only the cells on the periphery are in contact with the matrix, and only a subset of these cells invade. To more easily examine heterogeneity in the migration response of breast cancer cells to high density collagen, we embedded MDA-MB-231 (MDA) cells at low seeding density as single cells. Over the course of seven days, individual cells underwent distinct migration behaviors and proliferated to form either collectively invasive or non-invasive clonal structures (Fig. 1A). Mouse 4T1 cells

also showed a similar response (Fig. 1B). We hypothesized that identifying the gene expression differences between these two naturally emerging phenotypes may provide insights into the key regulatory nodes that sustain them, as well as implicate targets for preventing or arresting invasion. Using our previously established method for labeling and sorting cells from 3D collagen culture on the basis of phenotypes, we analyzed the differentially expressed genes between the invasive and non-invasive breast cancer phenotypes that arise in high density collagen (Fig. 1 C, Table S1).

Pathway enrichment analysis of the differentially expressed (DE) genes identified several categories of significance, including annotations for RHOBTB2 GTPase Cycle (combined score = 683.14, adjusted p-value = 4.319e-11) and Folding of Actin by CCT/TriC (combined score = 318.68, adjusted p-value = 2.93e-6) (Fig. 1 D). Since Rho GTPase signaling regulates cell motility (28, 29), we sought to further investigate these genes, along with additional gene ontologies (GO) annotated for Rho GTPase signaling. The combined set of DE genes indicate distinct programs associated with invasive versus non-invasive cells (Fig. 1 E). Rho GPTase signaling and downstream effectors on actin cytoskeleton regulation and actomyosin contractility are shown in Fig. 1 F to illustrate this point. Manually curated genes (*Pak1ip, Rac1, Washc4, Lima1, Myo5a, Myo19, Myo1b, Myl12a, Cfl1*) that were not included in GO annotation, likely due to the bias towards more common genes (30, 31), are also included to further show the differential regulation of actin and contractility. Invasive cells differentially express genes encoding multiple guanine nucleotide exchange factors (GEFs) and GTPase-activating proteins (GAPs), which would be expected to promote more dynamic Rho GTPase signaling. The downstream cytoskeletal regulators expressed by invasive cells (*Diaph3, Lima1, Washc4, Wasf1, Pak2*) would be expected to promote actin polymerization and result in cell elongation (32–34). Conversely, *Cfl1* upregulated in non-invasive cells promotes actin depolymerization and severing (35). Additionally, actomyosin contractility genes upregulated in the invasive cells (*Rock2, Cdc42bpa, Myo6, Myo1b, Myo9a, Myo5a, Myo9b, Myh10*) would be expected to enhance motility by enabling cells to generate traction and migrate through the ECM (36–38). *Myo6, Myo9a,* and *Myo9b* have been implicated in promoting collective migration in 2D epithelial sheets (39–41), so our data supports extension of their role into 3D collective invasion as well. Intriguingly, expression of *Rac1* and *Rac2* was upregulated in the non-invasive phenotype. These results suggest that multiple *Cdc42*-pathway genes may act in concert with myosin genes to enable the 3D collective invasion program.

We noted that *Cdc42bpa,* the mRNA encoding the myotonic dystrophy kinase-related Cdc42-binding kinase α (MRCKα) , was upregulated in the invasive phenotype. *Cdc42bpa* has an iron response element in its 3' UTR and is known to colocalize with transferrin receptor 1 (*Tfrc*) (42, 43), which prompted us to consider a potential link between the invasive cytoskeletal regulatory program and iron regulation. As an initial test to determine whether a link to iron may be worth investigating, we asked whether MRCKα is a critical regulator of collective migration. Addition

of the potent and selective MRCKα/□ inhibitor BDP-9066 to MDA and 4T1 cells embedded in Col1 significantly inhibited collective invasion, decreasing the percentage of invasive structures from 67.07% to 3.18% in MDAs ($p < 0.0001$) and from 64.17% to 24.92% invasive in 4T1s ($p = 0.0098$) (Fig. 1 G, H). These results indicate that MRCK, an iron-dependent cytoskeletal regulator, plays an important role in dictating the invasiveness of cancer cells.

Iron sequestration versus utilization programs differentiate non-invasive from invasive cells and predict patient survival

To further explore the role of iron in collective migration, differentially expressed genes linked to iron were identified through pathway enrichment (Iron Uptake and Transport, combined score = 11.27, adjusted p-value = 0.036), iron-related genesets from GSEA, and manual curation of recently identified iron-related genes (Fig. 2 A, Fig. S1). Invasive cells upregulated genes involved in iron uptake, including *Tfrc*, *Slc39a14,* and *Aco1*, while non-invasive cells upregulated genes involved in iron sequestration, such as *Fth1* and *Tmsb4x* (44). The strong enrichment of *Tfrc* in the invasive cells prompted us to assess genes whose expression is down-regulated by *Tfrc* knockout *(45)*. We found that the invasive phenotype is enriched for genes whose expression depends on *Tfrc* (Fig. 2 B). Together, these results suggest that differences in cytoplasmic iron levels regulated by distinct transcriptional programs may drive divergent migration outcomes.

Invasive collective migration requires OxPhos while non-invasive cells are more glycolytic

Invasive cells not only upregulated genes related to iron import, but also numerous protein-encoding genes that contain iron-sulfur clusters ([Fe-S]). Such proteins are crucial for cell metabolism, so we next analyzed the expression of genes related to glycolysis, OxPhos, and the TCA cycle. Multiple genes involved in OxPhos were differentially expressed between the two phenotypes (Fig. 2 C, Fig. S2), but glycolysis-related genes were preferentially upregulated in the non-invasive cell population (Fig. 2 D, Fig. S2). The only glycolysis-related genes upregulated in the invasive phenotype were *Fbp1*, which catalyzes a reverse step of glycolysis, and *Ldhb*, which preferentially promotes the conversion of lactate back to pyruvate (46). In contrast, the invasive cells upregulated genes involved in the TCA cycle (Fig. 2 E, Fig. S2), most notably *Aco1*. These genes indicate a program of anaplerotic fueling of the TCA cycle with glutamate via glutamine import and conversion (*Slc38a1*, *Gls*, *Got2*). All together, these results reveal intrinsic differences in iron-dependent metabolism that can emerge within a population of breast cancer cells to drive different phenotypes.

The divergent gene expression programs that emerge in HD Col1 are active in breast cancer patients

To assess the relevance of these modules to human breast cancer and clinical outcomes, we conducted survival curve analysis using the breast cancer RNA-seq dataset from the Km Plotter tool (47). The mean expression of the top iron-related genes from the non-invasive phenotype

(*Tmsb4x, B2m, Fth1, Ubb, Ubc, Atp6v0b*) are associated with improved overall survival (HR = 0.32) in triple negative breast cancer (TNBC) patients (Fig. 2 F). On the other hand, the top genes from the invasive phenotype (*Abce1, Ctlc, Aco1, Hif1a, Tfrc, Hspa9*) together predict worse survival (HR = 3.03) (Fig. 2 G). Analyzing these genes individually, we found that *Aco1* is significantly correlated with worse overall patient survival in all breast cancer patients (HR = 1.56, p = 0.00014) (Fig. 2 H), and TNBC patients had even worse outcomes when stratified by *Aco1* expression (Fig. 2 I) (HR = 4.22, p = 0.0041).

Histopathology of breast cancer patients obtained from the Human Protein Atlas also revealed protein expression profiles consistent with the cytoskeletal, iron, and metabolism gene modules of invasive and non-invasive cells (Fig. 2 J-K). Tumor sections from Patient 1910 revealed a protein expression pattern consistent with the invasive phenotype, while sections from Patient 4193 are strikingly similar to the non-invasive phenotype. The architectures of these two tumors also appear to mimic the *in vitro* phenotypes, which further supports the functional relevance of the distinct cytoskeletal programs. The linear chains of cells in the tumor of patient 1910 are reminiscent of the networks formed by collectively invasive cells *in vitro*, while the round cell clusters in the tumor of patient 4193 are reminiscent of the spheroids formed by non-invasive cells *in vitro*. These results suggest that the transcriptional and phenotypic heterogeneity induced in breast cancer cells by exposure to high density collagen *in vitro* closely mimics clinically relevant inter-patient heterogeneity.

<u>Computational modeling predicts iron-dependent effects on cell invasion by Eno1 and Aco1</u>
We next investigated how tumors may be switched away from the iron-utilization/invasive mode into the iron-sequestration/non-invasive mode, which is associated with TNBC patient survival. *Eno1,* which is upregulated in non-invasive cells, has recently been shown to have an iron-regulatory role via modulating the degradation of *Aco1*, which is upregulated in invasive cells (48). *Aco1,* also known as Iron Regulatory Protein 1 (*Irp1*), stabilizes *Tfrc* mRNA and decreases *Fth1* translation, thereby promoting iron import. Given this relationship, we examined the potential to modulate iron regulation and invasion through ENO1/ACO1 perturbation by developing a signaling network model of the two states (Fig. 3 A). ENO1 can interact with three upstream mediators, PI3K/AKT, AMPK/mTOR, and ACO1, affecting cell invasion (model output). As an iron regulator, ACO1 can induce variations in both cytosolic and metabolic iron levels, leading to changes in F-actin polymerization, ROS homeostasis, cell motility (49), and YAP/TAZ activation (50). As an initial model validation, we asked whether the model would predict a decrease in cell invasion after MRCK inhibition. Consistent with experimental data (Fig. 1 G-H), the model did successfully capture this relationship (Fig. 3 B). Next, we simulated ENO1 inhibition by altering its maximum activity from 1 to 0.1. The model predicts elevated cell invasion after ENO1 inhibition (Fig. 3 C).

To test the model predictions, we challenged both MDA-MB-231 and 4T1 cells with inhibitors targeting ENO1, which mediates glycolysis, or Complex I, which mediates oxidative

phosphorylation (Fig. 3 D-E). Complex I inhibitor rotenone stunted collective invasion, decreasing the percent of invasive structures from an average of 67.07% to 11.04% ($p < 0.0001$) in MDAs and from 64.17% to 7.14% in 4T1s ($p < 0.001$). Conversely, *Eno1* inhibitor AP-III-a4 increased the proportion of invasive structures in MDAs to 89.15% ($p = 0.0041$) and insignificantly increased the percentage of 4T1s to 76.76% ($p = 0.52$) . This indicates that the collective invasion phenotype is fueled by OxPhos, while non-invasive cells preferentially rely on glycolysis.

To better understand the mechanisms regulating cell invasion after ENO1 and MRCK inhibition, we used the model to predict the significant changes in signaling species mediating the impact of ENO1 (Fig. 3 F) and MRCK inhibition (Fig. 3 G) on cell invasion. After ENO1 inhibition, the model predicted a decrease in PI3K/AKT, mTOR and MMPs activities and an increase in AMPK activity which generally favor a decline in cell invasion. However, the increase in cytosolic and metabolic iron levels and subsequent increase in F-actin polymerization and ROS generation results in a net increase in cell invasion. The increase in cell invasion after ENO1 inhibition predicted by both model and experiments indicates a significant pro-invasive role of iron-dependent pathways after ENO1 inhibition. For MRCK inhibition, the model predicted a significant decrease in model species such as F-actin, YAP/TAZ, and cell motility which tend to reduce cell invasion as observed in the experiment (Fig. 1 G, H).

Although both the model and our experimental observations support the pro-invasive role of ENO1 inhibition, several studies have reported anti-invasive effects of ENO1 knockdown (51). We hypothesized that variations in cellular iron levels between different settings could affect cell invasion after ENO1 inhibition. Simulating cell invasion in control and ENO1 inhibited conditions for different cellular iron levels showed a positive relationship between iron level and invasive cell behavior. However, we observed an interesting response in the impact of ENO1 inhibition on cell invasion from pro-invasive to anti-invasive depending on cellular iron level (Fig. 3 H).

<u>Dense collagen I enhances the pro-invasion role of iron</u>

In addition to understanding how the two cell states are regulated, we also wanted to understand how dense Col1 initiates their spontaneous emergence. We wondered if these same cell states pre-existed and therefore could be identified independently of the high density Col1 system. If so, we would expect that culturing cells in different densities of Col1 should not affect iron-related gene expression patterns. Bulk RNA-sequencing of cells embedded in low density (LD) 2.5mg/ml or high density (HD) 6.0mg/ml Col1 after 24hrs in 3D culture revealed that iron uptake and utilization genes (including *Tfrc*, *Stead3*, *Slc11a2*, *Hmox1*, *Hif1α*) are higher in HD than LD. Conversely, iron storage genes are lower in the HD matrices, notably ferritin subunits *Fth1* and *Ftl* (Fig. 4 A). These results provide evidence that increasing Col1 density either lowers the availability of iron to these cells, or increases the demand for iron. To determine if increasing Col1 lowers the availability of iron, we assayed the iron levels in media following incubation

with varying Col1 concentrations. No significant differences in iron content were observed between Col1 concentrations after 6hr, 12hr, or 24hr (Fig. S3). Based on these findings, we hypothesized that the upregulation of iron-utilization genes is in response to a greater demand for iron by the cancer cells in HD matrices. To test this hypothesis, we measured cell motility in the LD and HD matrices in the presence of iron chelator deferoxamine (DFO) or supplemented iron in the form of $FeCl_3$. Cell trajectories were heterogeneous, where each treatment condition had both lowly and highly migratory cells (Fig. 4 B-C). The mean squared displacement (MSD) of both MDA and 4T1 cells in LD Col1 was unaffected by increasing iron levels, while iron chelation decreased motility (Fig. 4 D-E). On the other hand, cells in HD Col1 were more invasive in the presence of additional iron, and iron chelation dramatically reduced migration (Fig. 4 F-G). This data shows that iron is of particular importance for cells to migrate through more dense matrices, which coincides with an early shift in iron-related gene expression and the emergence of two distinct iron regulatory strategies associated with distinct migration strategies.

Heme oxygenase 1 is a critical source of endogenous iron for invasive migration

Among the most highly enriched genes from the 24hr RNA-sequencing in HD Col1 was *Hmox1*, which encodes for the enzyme heme oxygenase 1 (HO-1). HO-1 catabolizes heme into carbon monoxide (CO), biliverdin (BR), and iron. In this way, HO-1 impacts both iron availability and the redox state of the cell, as CO and BR have antioxidative properties. Given the iron-dependent increase in cell invasion, we hypothesized that HO-1 may provide an endogenous source of iron to promote cell invasion.

We found that *Hmox1* is upregulated between 24-72hr post-embedding in the HD Col1 matrices using RT-qPCR (Fig. 5 A). In addition, the heme analog cobalt protoporphyrin (CoPP) robustly induces and sustains *Hmox1* expression. Cell tracking showed that CoPP-induced *Hmox1* expression significantly increased the MSD and maximum cell invasion (Fig. 5 B-D). Additionally, CoPP rescued cell motility in the presence of DFO (Fig. 5 E-G), indicating that HO-1 expression may enhance motility by providing a critical source of intracellular iron for these cells.

We evaluated how HO-1 affects collective cell invasion by generating stable knockdowns of HO-1 (Fig. 5 H, Fig. S4). HO-1 knockdown (KD) formed significantly fewer collective invasion structures than the scramble controls (Fig. 5 I). Conversely, CoPP treatment increased invasion only in the scramble control cells, showing that the overexpression of HO-1 enhances collective invasion. We next sought to determine whether the pro-invasion effects of HO-1 are due to increased iron availability. Addition of iron to the media promoted invasion in both the control and HO-1 KD cells (Fig. 5 J-K). These findings show that HO-1 acts as a critical source of intracellular iron to fuel invasive migration, while a loss of HO-1 enriches for the non-invasive phenotype of breast cancer cells.

Discussion

Here, we show that exposure of breast cancer cells to dense Col1 can induce an "iron utilization and invasive" cell state or an "iron storage and non-invasive" cell state, both of which are physiologically relevant and represent distinct patient tumors with distinct outcomes. This supports accumulating evidence that microenvironmental factors can induce stable transcriptional responses that enable metastatic capabilities (13, 14). How exactly dense Col1 stimulates this response remains unclear. Prior studies indicate that cells embedded in dense Col1 are confined and show signs of increased ROS linked to low adhesion stress (27). Alternatively, ROS may be generated by the rupture of Col1 under tensile loads, which may be more likely in high density Col1 than low density Col1 matrices (52). The ROS generated by Col1 rupture can be converted to hydrogen peroxide or quinones; the former is a potent cell signaling molecule and the latter may induce collagen to form complexes with iron (53). Both species may help explain the early increase in *Hmox1* expression that we observed in breast cancer cells exposed to HD Col1 matrices.

Our results show that the early and transient induction of HO-1 expression can promote collective invasion in breast cancer cells by increasing labile iron, which feeds back on and coordinates metabolic and cytoskeletal gene modules that are part of an "iron utilization" program. KD of HO-1 and chelation of iron both induce a non-invasive cell state that can be rescued by supplementation with iron. However, HO-1 may play a role in the induction of the "iron storage and non-invasive" cell state that emerges in HD Col1 as well. Both cytosolic iron depletion and iron accumulation strategies could be responses to an imbalance in cellular ROS. HO-1 is most often viewed as a mediator of the cellular antioxidative response, but it can also promote reactive oxygen species (ROS) production through the Fenton Reaction by releasing intracellular labile iron. In line with this idea, previous reports suggest that HO-1 can play both pro- and anti- tumorigenic and metastatic roles (54–59), and our model predicts that such contradictory results can arise due to environment-dependent factors that impinge on intracellular iron levels.

Iron connects to the invasive machinery of breast cancer cells through the cdc42 signaling pathway. In particular, invasive cells upregulated two genes encoding subunits of MRCK (*Cdc42bpa* and *Cdc42bpb*), which in addition to promoting cytoskeletal contractility (60, 61), also its mRNA is stabilized by iron and its presence promotes transferrin-mediated iron import (42). We found that MRCK activity is necessary for collective invasion, and inhibiting its activity converts cells into a non-invasive phenotype. Conversely, non-invasive cells upregulated the expression of Rho GTPases *Rac1* and *Rac2* and NADPH oxidase (NOX) *Nox5,* which can interact to produce ROS (62) and may serve to balance the effect of their iron-sequestering gene program.

Iron levels and ROS also connect to the metabolic machinery. Higher ROS levels can rewire cells towards mitochondrial ATP production (63), which is a more iron-dependent process than glycolysis. We found that the "iron utilization and invasive" program relies heavily on OxPhos rather than glycolysis, and inhibition of OxPhos halted collective invasion. Furthermore, inhibiting the glycolytic enzyme ENO1 promoted the invasive phenotype. While cancer cells are typically more glycolytic, our findings support emerging evidence that more metastatic cells rely on OxPhos (64). ENO1, which is upregulated by non-invasive cells, has recently been shown to promote the degradation of ACO1(48), which is upregulated by invasive cells. Therefore, inhibition of ENO1 may promote invasion through its regulation of ACO1 expression. ACO1 is bi-functional, regulating the expression of genes involved in iron uptake, sequestration, and utilization as well as binding iron-sulfur clusters to promote its aconitase activity (65–68). Here, we show that upregulation of ACO1 may serve to link intracellular iron levels, metabolic strategies, and invasion in breast cancer. Indeed, high ACO1 expression strongly predicted poor survival in breast cancer patient data, particularly in TNBC. Interestingly, ACO2 has been shown to promote colon cancer progression (69). Our results implicate ACO1 in breast cancer and add important nuance to the idea that cancer cells become "iron-addicted" (70–74). Therapies aiming at either removing or over-loading iron in the tumor microenvironment are both being explored (72, 73). Our findings and model lend new insight into which tumors may respond to such therapies and implicate new potential targets. They also have implications for understanding how cancer cells could circumvent therapies that attempt to induce ferroptosis (75).

In summary, our findings add important systems biology insights to the emerging body of evidence that implicates cellular energetic states as critical determinants of metastasis (76–78). Cell migration is a metabolically-demanding behavior, so identifying unique energetic dependencies of collectively invasive cancer cells could lead to more effective therapies targeting metastasis (77).

Materials and Methods

Cell Culture

MDA-MB-231 (RRID:CVCL_0062), 4T1 (RRID:CVCL_0125), and LentiX cells (ATCC, Manassas, VA) were cultured at 37°C and 5% CO2 in high glucose Dulbecco's Modified Eagle Medium (Gibco Cat# 11995065) supplemented with 10% (v/v) fetal bovine serum (Corning Cat# 35010CV) and 0.1% (v/v) gentamicin (ThermoFisher Cat# 15750-060). Cells were passed when they reached 80% confluency.

Bulk RNA Sequencing Heat Map

RNA sequencing and data processing was performed previously by our lab (21). Briefly, cells were isolated from LD and HD Col1 matrices after 24hr in culture. Total RNA was sequenced on the Illumina MiSeq platform (Illumina, San Diego), reads were aligned using Bowtie2

(RRID:SCR_016368) and eXpress, and genes were mapped to the human genome hg19UCSC. Iron-related genes were identified using gene lists available from MSigDB (http://www.gsea-msigdb.org/gsea/index.jsp).

Cell Tracking

Live cell tracking was performed using a Nikon Ti Eclipse Inverted Epiflourescent microscope equipped with an incubation system to maintain 37°C, 5% CO2, and humidity. Bright field images were acquired using a 10x objective at 10 minute intervals. Cell tracking analysis was performed using Metamorph Software (RRID:SCR_002368, Molecular Devices, San Jose, CA) to generate xy-trajectories, followed by a custom MATLAB (RRID:SCR_001622, Mathworks, Natick, MA) script to calculate the migration parameters. MSDs were plotted using the first third of possible tau values. Max invasion distance was calculated as the maximum linear distance traveled from each cell's starting position.

Collective Migration Phenotype Quantification

Cells were cultured in the HD matrices for seven days and representative images from each individual gel were acquired on the same microscope described above. At this point the cells have formed distinct collective structures, which are outlined and shape descriptors are calculated using ImageJ (FIJI) (RRID:SCR_002285) (79). The ferret diameter of multicellular structure was used to report the invasion distance. Structures with a circularity index greater than 0.7 are considered non-invasive, while scores lower than 0.7 are considered invasive.

Lentiviral Transduction:

Lentiviral transduction of shRNA targeting hmox1 was completed following viral preparation using plasmids supplied by the La Jolla Institute for Immunology (Seq1: TRCN0000045250: ACAGTTGCTGTAGGGCTTTAT, Seq2: TRCN0000045251: CAACAAGGAGAGCCCAGTCTT) and gifted from Didier Trono (RRID:Addgene_12259, RRID:Addgene_12260). shRNA plasmids were cotransfected with the packaging and envelope plasmids using Lipofectamine 3000 at a ratio of 4:3:1 (#L3000001, Thermofisher) into LentiX cells. After 48hrs the media containing the lentivirus was collected and filtered through a 0.45µm filter. MDA-MB-231 cells were transduced with the lentivirus for 48hr, followed by selection with 1µg/mL puromycin (Millipore Sigma Cat# P9620). Protein-level knockdown was validated with a western blot.

3D collagen gels

Collagen matrices with embedded cells were made as previously described (21). Briefly, cells were mixed with reconstitution buffer and unpolymerized rat tail collagen I (#CB354249, Corning, Corning, NY) to reach the desired collagen concentration, followed by the addition of 1N NaOH to initiate polymerization. After 30 minutes at 37°C, media was added onto the polymerized gels. Media was changed every two days for the duration of the cultures. CoPP was

supplied by Enzo LifeSciences (Cat# ALX-430-076-M025, Farmingdale, NY) and resuspended in DMSO (Sigma Aldrich, St. Louis, MI). DFO (Cat# D9533) and $FeCl_3$ (Cat# 157740) were supplied by Sigma Aldrich (St. Louis, MI) and resuspended in dH20. Inhibitors rotenone (Cat# HY-B1756), AP-III-a4 (Cat# HY-15858), and BDP9066 (Cat# HY-111424) were purchased from MedChemExpress (Monmouth Junction, NJ).

Western Blotting

Western blot samples were prepared as previously described. Briefly, collagen gels were washed with ice cold PBS then scooped into protein low-bind tubes and placed on ice. RIPA lysis buffer (ThermoFisher Cat# 89900) with 1x protease and phosphatase inhibitors (ThermoFisher Cat# 78446) was added at an equal volume as that of the gels. After a brief 30 second sonication on ice, loading buffer (ThermoFisher Cat# B0007) was added to the gels to reach 1x concentration. Samples were incubated on ice for an hour, with vortexing every 15 minutes. Finally, samples were incubated at 95C for 5 minutes and stored at -20C until use. Proteins were separated in 10% SDS-PAGE gels and transferred to 0.45um PVDF membranes in 20% methanol Towbin buffer. Membranes were blocked with 5% BSA and incubated with primary antibodies for HMOX1 (Abcam Cat# ab52947, RRID:AB_880536) or GAPDH (Cell Signaling Technologies Cat# 2118S) overnight at 4°C. Washing was done 3x with TBST before and after secondary antibodies (Cell Signaling Technology Cat# 7074, RRID:AB_2099233) were added. ECL was added before visualization in a gel reader.

Single cell RNA Sequencing

Phenotypically-supervised single-cell RNA sequencing data comes from previous work by our lab (28). Briefly, cells expressing the photo-convertible fluorescent protein Dendra-2 Lifeact were imaged after 7 days and the phenotype of interest was converted from GFP to RFP. Cells were then isolated and sorted by FACS prior to sequencing. scRNA-seq was performed using the Illumina NovaSeq 6000 and analyzed using the cellRanger pipeline, aligning to reference human genome GRCh38.

Pathway enrichment analysis

Differentially expressed genes were determined using the non-parametric Wilcoxon rank sum test with a Bonferroni adjusted p-value < 0.05. Pathway enrichment analysis on the 1,706 DE genes was performed using the Reactome 2022 database on the Enrichr platform (80–82). The "combined score" enrichment value is calculated by taking the log of the p-value from the Fisher exact test and multiplying that by the z-score of the deviation from the expected rank.

RT-qPCR

MDA-MB-231 cells were embedded in 200uL HD Col1, then samples were treated with equal volume of Trizol (#15596026) at the specified timepoints. RNA was extracted using the Roche High Pure RNA Isolation Kit (#11828665001), and cDNA was created using SuperScript III reverse transcriptase (#18080044, Invitrogen). Taqman probes for *hmox1* (Hs01110250_m1) and *actb* (Hs01060665_g1) were used for qPCR in a QuantStudio3 thermocycler (ThermoFisher). Relative gene expression was calculated from $2^{-\Delta\Delta Ct}$ relative to vehicle control on Day 0.

Kaplan-Meier Plots

Kaplan-Meier plots were generated using the online Kaplan-Meier Plotter tool (kmplot.com) (47). This tool manually curates patient survival data from TCGA, EGA, and GEO and combines gene expression with clinical data. All analyses used RNA-seq data of breast cancer patient overall survival. The mean expression of the top six iron-related genes in the non-invasive and invasive phenotypes for triple negative breast cancer patients was used for the plots in Figure 1. Analyses for *Aco1* expression for overall survival were run on RNA-seq data on two groups of patient samples split by quantile expressions. Hazard ratio is shown with 95% confidence interval, along with the logrank P value.

Cancer Patient Histological Data

Histology of breast cancer patients was obtained by searching the Human Protein Atlas (HPA) online database for proteins encoded by differentially expressed genes identified using PhenoSeq (https://www.proteinatlas.org/humanproteome/pathology) (83). Patient 1910 and Patient 4193 were selected for analysis because they were stained for many of the same proteins, which also were relevant to our results. Antibodies that were not specific to different isoforms are labeled for both possible proteins, which was the case for UBB/UBC and RAC1/RAC2. Patient 4193 did not have sections stained for TFRC or ACO1.

Model Development

By identifying the main iron-dependent and independent pathways that could transduce the perturbations of Eno1 to cell invasion from the literature, we developed a signaling network model linking Eno1 to cell invasion. In total, the model includes 26 species and 45 reactions

(Table S5). We employed a normalized-Hill logic-based ODE approach (84) to convert the interaction between signaling species to a system of ordinary differential equations. For example, if signaling node A activates or inhibits D, the variation of D in time will be calculated in the following way.

$$dD/dt = (1/T_D).(W_R \,.\, f_{act/inh}\,(A).D_{max} - D)$$
$$f_{act}\,(A) = B.A^n/(K^n + A^n); f_{inh}\,(A) = 1 - B.A^n/(K^n + A^n);\ where$$
$$B = (EC_{50}{}^n - 1)/(2EC_{50}{}^n - 1);\ K = (B-1)^{1/n}$$

Six default parameters adjust the activity of signaling species in the model. Hill equation parameters include EC50 (default = 0.5) and n (default = 1.4). W_R (default = 0.5) is the reaction weight determining the strength of each reaction in the model. "Dmax" (default = 1) determines the maximum activity of each species and was set to 0.1 for simulating the inhibition. "T" represents the time constant (default = 1) of each species respectively (84).

We added a noise term □(t) in the equation of each species to include their noise in experiments. The noise terms were modeled by the Ornstein–Uhlenbeck process:

$$\boldsymbol{\tau}^{noise} d\boldsymbol{\eta} \quad = -\boldsymbol{\eta} dt + \boldsymbol{\sigma} dW_t$$

Where □□□□□□ and □ are noise timescale and amplitude, respectively. □□'s are identically distributed Weiner processes independent for each species (85). □(t) has a zero mean and □^{2}/(2□□□□□□) variance. □□□□□□ was selected equal to one for model simulations. By using the Milstein scheme (86), we numerically solved the noise term □, and used the Euler scheme to solve the dynamics of signaling species on the simulation time interval.

$$dy/dt = f_{deterministic}(y) + \boldsymbol{\eta}$$

For more information please see (87).

<u>Simulating Experiment</u>

To determine the initial condition (control state) of the cells, we simulated the model without any input (change in ENO1 activity) to reach the steady state. All model parameters were selected by their default values except W_R of two negative feedback reactions from cytosolic Fe to ENO1 and ACO1, which were set to a lower value of 0.2 to prevent the oversaturation of model species. Notably, as the default parameters were selected for the model due to a lack of data, only qualitative comparisons of model predictions with experiments are possible. As the sensitivity of model species to the upstream signal is negatively associated with the number of mediators in each pathway, we set a W_R of the ENO1-ACO1 reaction equal to 1 to have comparable impacts on cell invasion from different pathways. Forty (40) *in silico* replicates were simulated per condition with a noise amplitude of □ equal to 0.2. The median coefficient of variation for model species was calculated as 5%, which is in the range of experimental data (88). MATLAB R2021 was used for all numerical simulations.

Acknowledgements

Support for this study was provided by National Science Foundation CAREER award MCB-1651855 (S.I.F.), National Science Foundation grant DMS-1953469, National Cancer Institute grant CA274502, American Cancer Society Research Scholar Grant RSG-21-033-01-CSM (S.I.F.), Wu Tsai Human Performance Alliance (S.I.F. and P.R.), and AHA Postdoctoral fellowship (A.K.). We would like to thank the UC San Diego School of Medicine Microscopy Core, which is supported by the National Institute of Neurological Disorders and Stroke grant P30NS047101.

Author Contributions

W.D.L. designed experiments, conducted experimentation, analyzed data, and contributed to the writing of the manuscript. S.I.F. conceived of the project, assisted in experimental design and interpretation, and contributed to the writing of the manuscript. A.K. and P.R. developed and implemented the signaling model and contributed to data interpretation and writing the manuscript.

Conflict of Interest Statement

The authors declare no potential conflicts of interest.

Figure Captions

Figure 1: Distinct cytoskeletal programs underlie breast cancer migration heterogeneity, with MRCK serving as a critical regulatory node of collective invasion.
(A-B) Representative micrographs of MDA-MB-231 (A) and 4T1 (B) collective migration phenotypes that form when single cell suspensions embedded in 6mg/ml collagen I are cultured for one week. Red arrows point to the invasive phenotype, while the blue arrows show the non-invasive spheroidal structures. **(C)** Schematic of phenotypically-supervised single cell RNA sequencing (PhenoSeq). Single cell suspensions are embedded in 6mg/ml Col1 and cultured for seven days, where they form both invasive and non-invasive collective migration phenotypes. Photoconversion of cells from each population enables subsequent sorting and sequencing while retaining knowledge of the cell's phenotype. This labeling enables clustering based on phenotype, which reveals distinct gene expression patterns that algorithm-based unsupervised clustering misses. **(D)** Pathway enrichment analysis using the Reactome 2022 database of all differentially expressed genes found in the MDA-MB-231 PhenoSeq data. **(E)**Volcano plot of differential gene expression between cells in the collective non-invasive and invasive phenotypes related to Rho GTPase signaling. **(F)** Diagram showing Rho GTPase signaling and the downstream effects on actin cytoskeleton regulation and actomyosin contractility. The MRCKα-encoding gene *Cdc42bpa* contains an iron responsive element in the 3' UTR of the mRNA. **(G-H)** Representative micrographs show that inhibition of MRCK with 0.5μM BDP-9066 diminishes the collective invasion phenotype in both MDAs (G) and 4T1s (H). Quantification

shows the percent of collective migration structures with either phenotype within each biological replicate. Scale bar = 200μm. N = 3 biological replicates per treatment group. Statistical significance was determined using a student's t-test. * $p < 0.05$, ** $p < 0.01$, *** $p < 0.001$, **** $p < 0.0001$.

Figure 2: Iron sequestration versus utilization programs differentiate non-invasive from invasive cells and predict patient survival

(A) Differentially expressed genes identified from PhenoSeq that are related to intracellular iron usage. **(B)** Genes whose expression decreases when *Tfrc* is knocked down are enriched in the invasive phenotype. **(C-E)** Differentially expressed genes related to (C) OxPhos, (D) glycolysis, and (E) TCA cycle. **(F-G)** Kaplan Meier plots showing TNBC patient five-year overall survival stratified by high or low mean expression of the top six iron-related genes enriched in the (F) non-invasive or (G) invasive populations. **(H-I)** Kaplan Meier five-year overall survival plots for (H) all breast cancer patients or (I) TNBC patients stratified by *Aco1*. **(J-K)** Breast cancer tumor sections of Patient 1910 and Patient 4193 from the HPA show gene expression patterns matching the (J) divergent metabolism and (K) cytoskeletal regulation programs identified from the collective non-invasive and invasive phenotypes. Protein expression from Patient 1910 is consistent with the invasive phenotype, while Patient 4193 is consistent with the non-invasive phenotype.

Figure 3: Computational modeling predicts iron-dependent effects on cell invasion by Eno1 and Aco1

(A) The network model of Eno1-mediated cell invasion. Solid arrows indicate cellular species' activation (↓) or inhibition (⊥). Dashed arrows illustrate the feedback. **(B)** The model reproduces a decrease in cell invasion after MRCK inhibition and **(C)** predicts an increase after Eno1 inhibition. **(D-E)** Representative images of cells treated with 0.1% DMSO vehicle, 1μM complex I inhibitor rotenone, or 1μM glycolytic enzyme ENO1 inhibitor AP-III-a4. Inhibition of complex I abrogated the collective invasion phenotype, while inhibition of ENO1 decreased the proportion of the non-invasive phenotype in both MDAs (E) and 4T1s (F). Quantification shows the percent of collective migration structures with either phenotype within each biological replicate. Scale bar = 200μm. N = 3 biological replicates per treatment group. Statistical significance was determined using one-way ANOVA followed by a Dunnett post-test comparing each treatment group to the vehicle group. * $p < 0.05$, ** $p < 0.01$, *** $p < 0.001$, **** $p < 0.0001$. **(F-G)** Model predictions of the mechanism and significant mediators linking the perturbations to cell invasion following (F) ENO1-inhibition or (G) MRCK-inhibition.**(H)** Simulated impact on cell invasion for different iron levels following ENO1-inhibition shows a decrease in cell motility at low iron levels and an increase at higher iron concentrations. N = 30 *in silico* replicates.

Figure 4: Iron promotes invasive cell migration in a collagen density-dependent manner

(A) Bulk RNA-sequencing of MDA-MB-231 cells embedded in 2.5mg/ml (LD) or 6mg/ml (HD) collagen I matrices for 24hr reveals differential expression of iron-related genes. Cells in the HD matrices are enriched for genes related to iron import and usage, while those in LD matrices are enriched for genes related to iron sequestration or storage. Color gradient corresponds to mean z-score of the transcripts per million (TPM) for each gene in the two conditions. N = 3 biological replicates per condition. **(B-C)** Cell tracking trajectories of MDA-MB-231 (B) and 4T1 (C) cells embedded in LD or HD matrices between 24-48hr post-embedding. Cells were treated with vehicle (0.1% dH_20), 10µM DFO, or 200µM $FeCl_3$. N = 3 biological replicates with at least n = 30 cells per replicate. Scale bar = 50µm. **(D-G)** Mean squared displacement (MSD) and max invasion measurements of the cell tracking data in LD matrices for MDA-MB-231 (D) and 4T1 (E) cells show that chelation of iron by DFO decreases overall migration and invasion, while treatment with $FeCl_3$ did not significantly change the migration behavior. In the HD matrices, both MDA-MB-231 (F) and 4T1 (G) cells increased their motility and invasion when treated with $FeCl_3$, while DFO treatment had a similar effect as that in the LD matrices. Statistical significance was determined using one-way ANOVA followed by a Dunnett post-test. * $p < 0.05$, ** $p < 0.01$, *** $p < 0.001$, **** $p < 0.0001$

Figure 5: Heme oxygenase I promotes cell invasion through iron

(A) RT-qPCR analysis of *hmox1* gene expression in HD Col1 matrices shows a peak between 24-72hr for MDA-MB-231 cells. Treatment with 10µM cobalt protoporphyrin (CoPP) induces *hmox1* expression approximately 25x higher than levels measured 1hr after embedding. *hmox1* gene expression normalized to *actb* transcript levels. **(B-D)** Trajectories of cells treated with CoPP compared to vehicle controls (B) reveal significant increases in motility (C) and invasion (D). N = 3 biological replicates with n = 30 trajectories per replicate. **(E)** Brightfield images of MDAs after 48hr culture in HD matrices treated with either DFO or DFO+CoPP show the preservation of cell elongation by CoPP. scale bar = 200µm. **(F-H)** Cell trajectories and migration analysis shows the protective effects of CoPP treatment when cells were challenged with DFO. N = 3 biological replicates with n = 30 trajectories per replicate. **(I-J)** Knockdown of *hmox1* by shRNA results in less collective cell invasion, while CoPP treatment enhances collective invasion only for the scramble control population. $N \geq 3$ biological replicates for each condition. **(K-L)** Supplementation of $FeCl_3$ to culture media of cells embedded in HD Col1 increases collective invasion in scramble controls and HO-1 KD cells. $N \geq 3$ biological replicates for each condition scale bar = 50µm for trajectories and 200µm for images. Statistical significance was determined by one-way ANOVA followed by Dunnett post-test for (D) and (H), and two-way ANOVA followed by Sidák post-test for (J) and (L). * $p < 0.05$, ** $p < 0.01$, *** $p < 0.001$, **** $p < 0.0001$

Supplemental Information

Figure S1: Schematic representation of the protein function of differentially expressed iron-related genes

Iron import into cells is mediated via the ion transporters DMT1, SLC39A14, or transferrin (TF) binding to transferrin receptor (TFRC) and endocytosis. Labile iron is present in cells at low concentrations, but is typically incorporated into iron-containing proteins that are necessary for cell functions including DNA synthesis and repair, translation, and metabolism. Iron can also be sequestered and stored, canonically by ferritin, though other proteins have iron chelation properties. Heme oxygenase I enzymatic degradation of heme provides another source of intracellular iron.

Figure S2: Schematic representation of the protein function of differentially expressed metabolism genes

Essential proteins involved in glucose metabolism through glycolysis, the TCA cycle, and oxidative phosphorylation. Shunting from glycolysis to the pentose phosphate pathway is also shown, as are anapleirotic sources of the TCA cycle.

Figure S3: Collagen I density does not alter iron levels in media

Iron concentrations remain consistent between media samples incubated with 1mg/ml, 2.5mg/ml, or 6mg/ml collagen I matrices for 6, 12, or 24hr. Iron concentration was determined using the Colorimetric Iron Assay Kit from Abcam (Cambridge, Ma).

Figure S4: Knockdown of HO-1 using shRNA

(A) Western blot for HO-1 in wild-type (WT) MDAs and MDAs lentivirally transduced with shRNA targeting a scramble sequence (shSCR) or *Hmox1* (shHMOX1). Cells were cultured in 100µm CoPP to induce HO-1 protein expression.

Table S1 - scRNA-sequencing results.

Table S2 - Rho GTPase and actin-regulating DE genes

Table S3 - Iron DE genes

Table S4 - Metabolism DE genes

Table S5 - Model Parameters and Reactions

References:

1. H. Dillekå, M. S. Rogers, O. Straume, Are 90% of deaths from cancer caused by metastases? *Cancer Med.* **8**, 5574–5576 (2019).

2. A. Wells, J. Grahovac, S. Wheeler, B. Ma, D. Lauffenburger, Targeting tumor cell motility as a strategy against invasion and metastasis. *Trends Pharmacol. Sci.* **34**, 283–289 (2013).

3. T. D. Palmer, W. J. Ashby, J. D. Lewis, A. Zijlstra, Targeting tumor cell motility to prevent metastasis. *Adv. Drug Deliv. Rev.* **63**, 568–581 (2011).

4. K. Ganesh, J. Massagué, Targeting metastatic cancer. *Nat. Med.* **27**, 34–44 (2021).

5. S. A. Patel, P. Rodrigues, L. Wesolowski, S. Vanharanta, Genomic control of metastasis. *Br. J. Cancer* **124**, 3–12 (2021).

6. P. Priestley, *et al.*, Pan-cancer whole-genome analyses of metastatic solid tumours. *Nature* **575**, 210–216 (2019).

7. S. Turajlic, C. Swanton, Metastasis as an evolutionary process. *Science* **352**, 169–175 (2016).

8. B. Vogelstein, *et al.*, Cancer genome landscapes. *Science* **339**, 1546–1558 (2013).

9. P. Rodrigues, *et al.*, NF-κB--Dependent Lymphoid Enhancer Co-option Promotes Renal Carcinoma MetastasisCross-Lineage Enhancer Co-option Promotes RCC Metastasis. *Cancer Discov.* **8**, 850–865 (2018).

10. K. Ganesh, *et al.*, Author Correction: L1CAM defines the regenerative origin of metastasis-initiating cells in colorectal cancer. *Nat Cancer* **1**, 1128 (2020).

11. R. Eyre, *et al.*, Microenvironmental IL1β promotes breast cancer metastatic colonisation in the bone via activation of Wnt signalling. *Nat. Commun.* **10**, 5016 (2019).

12. N. Mohammadi Ghahhari, *et al.*, Cooperative interaction between ERα and the EMT-inducer ZEB1 reprograms breast cancer cells for bone metastasis. *Nat. Commun.* **13**, 2104 (2022).

13. A. A. Chakraborty, *et al.*, Histone demethylase KDM6A directly senses oxygen to control chromatin and cell fate. *Science* **363**, 1217–1222 (2019).

14. C. Wiel, *et al.*, BACH1 stabilization by antioxidants stimulates lung cancer metastasis. *Cell* **178**, 330–345.e22 (2019).

15. D. A. Lawson, K. Kessenbrock, R. T. Davis, N. Pervolarakis, Z. Werb, Tumour heterogeneity and metastasis at single-cell resolution. *Nat. Cell Biol.* **20**, 1349–1360 (2018).

16. K. J. Cheung, A. J. Ewald, A collective route to metastasis: Seeding by tumor cell clusters. *Science* **352**, 167–169 (2016).

17. P. Friedl, D. Gilmour, Collective cell migration in morphogenesis, regeneration and cancer. *Nat. Rev. Mol. Cell Biol.* **10**, 445–457 (2009).

18. K. J. Cheung, E. Gabrielson, Z. Werb, A. J. Ewald, Collective invasion in breast cancer requires a conserved basal epithelial program. *Cell* **155**, 1639–1651 (2013).

19. N. Aceto, *et al.*, Circulating tumor cell clusters are oligoclonal precursors of breast cancer metastasis. *Cell* **158**, 1110–1122 (2014).

20. A. Haeger, M. Krause, K. Wolf, P. Friedl, Cell jamming: collective invasion of mesenchymal tumor cells imposed by tissue confinement. *Biochim. Biophys. Acta* **1840**, 2386–2395 (2014).

21. D. O. Velez, *et al.*, 3D collagen architecture induces a conserved migratory and transcriptional response linked to vasculogenic mimicry. *Nat. Commun.* **8**, 1651 (2017).

22. S. K. Ranamukhaarachchi, *et al.*, Macromolecular crowding tunes 3D collagen architecture and cell morphogenesis. *Biomaterials science* **7**, 618–633 (2019).

23. N. F. Boyd, *et al.*, Mammographic breast density as an intermediate phenotype for breast cancer. *Lancet Oncol.* **6**, 798–808 (2005).

24. N. F. Boyd, *et al.*, Mammographic density and the risk and detection of breast cancer. *N. Engl. J. Med.* **356**, 227–236 (2007).

25. J. J. Northey, *et al.*, Stiff stroma increases breast cancer risk by inducing the oncogene ZNF217. *J. Clin. Invest.* **130**, 5721–5737 (2020).

26. M. J. Paszek, *et al.*, Tensional homeostasis and the malignant phenotype. *Cancer Cell* **8**, 241–254 (2005).

27. D. O. Velez, *et al.*, 3D collagen architecture regulates cell adhesion through degradability, thereby controlling metabolic and oxidative stress. *Integr. Biol.* **11**, 221–234 (2019).

28. K. Chen, *et al.*, Phenotypically supervised single-cell sequencing parses within-cell-type heterogeneity. *iScience* **24**, 101991 (2021).

29. K. Chen, *et al.*, A phenotypically supervised single-cell analysis protocol to study within-cell-type heterogeneity of cultured mammalian cells. *STAR Protoc* **2**, 100561 (2021).

30. C. Dessimoz, N. Škunca, *The gene ontology handbook* (Springer Nature, 2017).

31. A. Tomczak, *et al.*, Interpretation of biological experiments changes with evolution of the Gene Ontology and its annotations. *Sci. Rep.* **8**, 5115 (2018).

32. L. Dong, *et al.*, DIAPH3 promoted the growth, migration and metastasis of hepatocellular

carcinoma cells by activating beta-catenin/TCF signaling. *Mol. Cell. Biochem.* **438**, 183–190 (2018).

33. R. S. Maul, *et al.*, EPLIN regulates actin dynamics by cross-linking and stabilizing filaments. *J. Cell Biol.* **160**, 399–407 (2003).

34. H. Phee, *et al.*, Pak2 is required for actin cytoskeleton remodeling, TCR signaling, and normal thymocyte development and maturation. *Elife* **3**, e02270 (2014).

35. E. Nishida, S. Maekawa, H. Sakai, Cofilin, a protein in porcine brain that binds to actin filaments and inhibits their interactions with myosin and tropomyosin. *Biochemistry* **23**, 5307–5313 (1984).

36. S. Liu, The ROCK signaling and breast cancer metastasis. *Mol. Biol. Rep.* **38**, 1363–1366 (2011).

37. J. L. Ouderkirk, M. Krendel, Non-muscle myosins in tumor progression, cancer cell invasion, and metastasis. *Cytoskeleton* **71**, 447–463 (2014).

38. K. A. Makowska, R. E. Hughes, K. J. White, C. M. Wells, M. Peckham, Specific Myosins Control Actin Organization, Cell Morphology, and Migration in Prostate Cancer Cells. *Cell Rep.* **13**, 2118–2125 (2015).

39. C. Lei, *et al.*, miR-143 and miR-145 inhibit gastric cancer cell migration and metastasis by suppressing MYO6. *Cell Death Dis.* **8**, e3101 (2017).

40. T. Omelchenko, Regulation of collective cell migration by RhoGAP myosin IXA. *Small GTPases* **3**, 213–218 (2012).

41. F.-S. Yi, *et al.*, TSAd Plays a Major Role in Myo9b-Mediated Suppression of Malignant Pleural Effusion by Regulating TH1/TH17 Cell Response. *J. Immunol.* **205**, 2926–2935 (2020).

42. R. Cmejla, *et al.*, Human MRCKalpha is regulated by cellular iron levels and interferes with transferrin iron uptake. *Biochem. Biophys. Res. Commun.* **395**, 163–167 (2010).

43. P. Y. He, *et al.*, Inhibition of cell migration and invasion by miR-29a-3p in a colorectal cancer cell line through suppression of CDC42BPA mRNA expression. *Oncol. Rep.* **38**, 3554–3566 (2017).

44. J. I. Lachowicz, *et al.*, Thymosin β4 Is an Endogenous Iron Chelator and Molecular Switcher of Ferroptosis. *Int. J. Mol. Sci.* **23** (2022).

45. K. A. O'Donnell, *et al.*, Activation of transferrin receptor 1 by c-Myc enhances cellular proliferation and tumorigenesis. *Mol. Cell. Biol.* **26**, 2373–2386 (2006).

46. K. Urbańska, A. Orzechowski, Unappreciated Role of LDHA and LDHB to Control Apoptosis and Autophagy in Tumor Cells. *Int. J. Mol. Sci.* **20** (2019).

47. B. Győrffy, Survival analysis across the entire transcriptome identifies biomarkers with the highest prognostic power in breast cancer. *Comput. Struct. Biotechnol. J.* **19**, 4101–4109 (2021).

48. T. Zhang, *et al.*, ENO1 suppresses cancer cell ferroptosis by degrading the mRNA of iron regulatory protein 1. *Nat Cancer* **3**, 75–89 (2022).

49. G. Shenoy, *et al.*, Cellular iron status influences cell motility in glioblastoma. *Biophys. J.* **121**, 267a (2022).

50. W.-H. Yang, J.-T. Chi, Hippo pathway effectors YAP/TAZ as novel determinants of ferroptosis. *Mol Cell Oncol* **7**, 1699375 (2020).

51. C. K. Huang, Y. Sun, L. Lv, Y. Ping, ENO1 and Cancer. *Mol Ther Oncolytics* **24**, 288–298 (2022).

52. C. Zapp, *et al.*, Mechanoradicals in tensed tendon collagen as a source of oxidative stress. *Nat. Commun.* **11**, 2315 (2020).

53. M. J. Harrington, A. Masic, N. Holten-Andersen, J. H. Waite, P. Fratzl, Iron-clad fibers: a metal-based biological strategy for hard flexible coatings. *Science* **328**, 216–220 (2010).

54. B. Wegiel, Z. Nemeth, M. Correa-Costa, A. C. Bulmer, L. E. Otterbein, Heme oxygenase-1: a metabolic nike. *Antioxid. Redox Signal.* **20**, 1709–1722 (2014).

55. A. Jozkowicz, H. Was, J. Dulak, Heme oxygenase-1 in tumors: is it a false friend? *Antioxid. Redox Signal.* **9**, 2099–2117 (2007).

56. K. N. Luu Hoang, J. E. Anstee, J. N. Arnold, The Diverse Roles of Heme Oxygenase-1 in Tumor Progression. *Front. Immunol.* **12**, 658315 (2021).

57. H. Was, J. Dulak, A. Jozkowicz, Heme oxygenase-1 in tumor biology and therapy. *Curr. Drug Targets* **11**, 1551–1570 (2010).

58. Q. Li, *et al.*, Heme Oxygenase-1 Inhibits Tumor Metastasis Mediated by Notch1 Pathway in Murine Mammary Carcinoma. *Oncol. Res.* **27**, 643–651 (2019).

59. J.-R. Tsai, *et al.*, High expression of heme oxygenase-1 is associated with tumor invasiveness and poor clinical outcome in non-small cell lung cancer patients. *Cell. Oncol.* **35**, 461–471 (2012).

60. Z. Zhao, E. Manser, Myotonic dystrophy kinase-related Cdc42-binding kinases (MRCK), the ROCK-like effectors of Cdc42 and Rac1. *Small GTPases* **6**, 81–88 (2015).

61. S. Wilkinson, H. F. Paterson, C. J. Marshall, Cdc42-MRCK and Rho-ROCK signalling cooperate in myosin phosphorylation and cell invasion. *Nat. Cell Biol.* **7**, 255–261 (2005).

62. A. Acevedo, C. González-Billault, Crosstalk between Rac1-mediated actin regulation and

ROS production. *Free Radic. Biol. Med.* **116**, 101–113 (2018).

63. P. Romani, L. Valcarcel-Jimenez, C. Frezza, S. Dupont, Crosstalk between mechanotransduction and metabolism. *Nat. Rev. Mol. Cell Biol.* **22**, 22–38 (2021).

64. P. E. Porporato, *et al.*, A mitochondrial switch promotes tumor metastasis. *Cell Rep.* **8**, 754–766 (2014).

65. S. Kaptain, *et al.*, A regulated RNA binding protein also possesses aconitase activity. *Proc. Natl. Acad. Sci. U. S. A.* **88**, 10109–10113 (1991).

66. D. J. Haile, *et al.*, Cellular regulation of the iron-responsive element binding protein: disassembly of the cubane iron-sulfur cluster results in high-affinity RNA binding. *Proc. Natl. Acad. Sci. U. S. A.* **89**, 11735–11739 (1992).

67. C. C. Philpott, R. D. Klausner, T. A. Rouault, The bifunctional iron-responsive element binding protein/cytosolic aconitase: the role of active-site residues in ligand binding and regulation. *Proc. Natl. Acad. Sci. U. S. A.* **91**, 7321–7325 (1994).

68. O. Stehling, *et al.*, Human CIA2A-FAM96A and CIA2B-FAM96B integrate iron homeostasis and maturation of different subsets of cytosolic-nuclear iron-sulfur proteins. *Cell Metab.* **18**, 187–198 (2013).

69. M. Miyazawa, A. R. Bogdan, Y. Tsuji, Perturbation of Iron Metabolism by Cisplatin through Inhibition of Iron Regulatory Protein 2. *Cell Chem Biol* **26**, 85–97.e4 (2019).

70. S. V. Torti, F. M. Torti, Iron and cancer: 2020 vision. *Cancer Res.* **80**, 5435–5448 (2020).

71. D. H. Manz, N. L. Blanchette, B. T. Paul, F. M. Torti, S. V. Torti, Iron and cancer: recent insights. *Ann. N. Y. Acad. Sci.* **1368**, 149–161 (2016).

72. D. Basuli, *et al.*, Iron addiction: a novel therapeutic target in ovarian cancer. *Oncogene* **36**, 4089–4099 (2017).

73. P. Lelièvre, L. Sancey, J.-L. Coll, A. Deniaud, B. Busser, Iron dysregulation in human cancer: altered metabolism, biomarkers for diagnosis, prognosis, monitoring and rationale for therapy. *Cancers* **12** (2020).

74. J. Li, *et al.*, Identification of Iron Metabolism-Related Gene Signatures for Predicting the Prognosis of Patients With Sarcomas. *Front. Oncol.* **10**, 599816 (2020).

75. S. J. Dixon, *et al.*, Ferroptosis: an iron-dependent form of nonapoptotic cell death. *Cell* **149**, 1060–1072 (2012).

76. M. R. Zanotelli, *et al.*, Regulation of ATP utilization during metastatic cell migration by collagen architecture. *Mol. Biol. Cell* **29**, 1–9 (2018).

77. J. A. Mosier, S. C. Schwager, D. A. Boyajian, C. A. Reinhart-King, Cancer cell metabolic

plasticity in migration and metastasis. *Clin. Exp. Metastasis* **38**, 343–359 (2021).

78. M. R. Zanotelli, J. Zhang, C. A. Reinhart-King, Mechanoresponsive metabolism in cancer cell migration and metastasis. *Cell Metab.* **33**, 1307–1321 (2021).

79. J. Schindelin, *et al.*, Fiji: an open-source platform for biological-image analysis. *Nat. Methods* **9**, 676–682 (2012).

80. E. Y. Chen, *et al.*, Enrichr: interactive and collaborative HTML5 gene list enrichment analysis tool. *BMC Bioinformatics* **14**, 128 (2013).

81. M. V. Kuleshov, *et al.*, Enrichr: a comprehensive gene set enrichment analysis web server 2016 update. *Nucleic Acids Res.* **44**, W90–7 (2016).

82. Z. Xie, *et al.*, Gene Set Knowledge Discovery with Enrichr. *Curr Protoc* **1**, e90 (2021).

83. M. Uhlén, *et al.*, Proteomics. Tissue-based map of the human proteome. *Science* **347**, 1260419 (2015).

84. M. J. Kraeutler, A. R. Soltis, J. J. Saucerman, Modeling cardiac β-adrenergic signaling with normalized-Hill differential equations: comparison with a biochemical model. *BMC Syst. Biol.* **4**, 157 (2010).

85. E. Bibbona, G. Panfilo, P. Tavella, The Ornstein–Uhlenbeck process as a model of a low pass filtered white noise. *Metrologia* **45**, S117 (2008).

86. P. E. Kloeden, E. Platen, "Stochastic Differential Equations" in *Numerical Solution of Stochastic Differential Equations*, P. E. Kloeden, E. Platen, Eds. (Springer Berlin Heidelberg, 1992), pp. 103–160.

87. L. Qiao, *et al.*, A circuit for secretion-coupled cellular autonomy in multicellular eukaryotic cells. *Mol. Syst. Biol.* **19**, e11127 (2023).

88. K. M. Kovary, B. Taylor, M. L. Zhao, M. N. Teruel, Expression variation and covariation impair analog and enable binary signaling control. *Mol. Syst. Biol.* **14**, e7997 (2018).

Figure 1

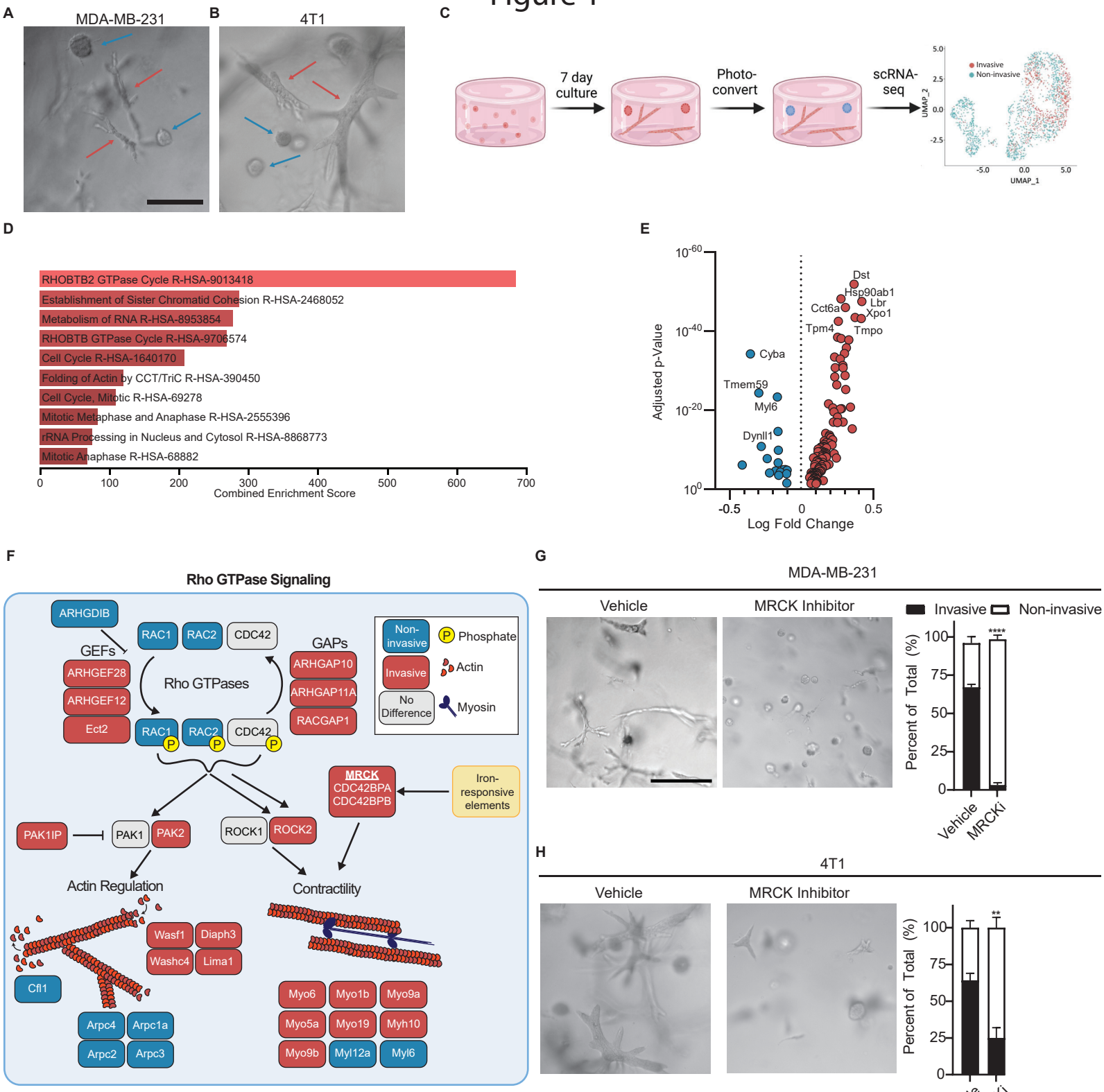
A
MDA-MB-231
B
4T1
C
7 day culture
Photo-convert
scRNA-seq
Invasive
Non-invasive
UMAP_2
UMAP_1
D
RHOBTB2 GTPase Cycle R-HSA-9013418
Establishment of Sister Chromatid Cohesion R-HSA-2468052
Metabolism of RNA R-HSA-8953854
RHOBTB GTPase Cycle R-HSA-9706574
Cell Cycle R-HSA-1640170
Folding of Actin by CCT/TriC R-HSA-390450
Cell Cycle, Mitotic R-HSA-69278
Mitotic Metaphase and Anaphase R-HSA-2555396
rRNA Processing in Nucleus and Cytosol R-HSA-8868773
Mitotic Anaphase R-HSA-68882
Combined Enrichment Score
E
Adjusted p-Value
Log Fold Change
Dst
Hsp90ab1
Lbr
Cct6a
Xpo1
Tpm4
Tmpo
Cyba
Tmem59
Myl6
Dynll1
F
Rho GTPase Signaling
ARHGDIB
GEFs
ARHGEF28
ARHGEF12
Ect2
RAC1
RAC2
CDC42
Rho GTPases
GAPs
ARHGAP10
ARHGAP11A
RACGAP1
Non-invasive
Invasive
No Difference
Phosphate
Actin
Myosin
MRCK
CDC42BPA
CDC42BPB
Iron-responsive elements
PAK1IP
PAK1
PAK2
ROCK1
ROCK2
Actin Regulation
Contractility
Wasf1
Diaph3
Washc4
Lima1
Cfl1
Arpc4
Arpc1a
Arpc2
Arpc3
Myo6
Myo1b
Myo9a
Myo5a
Myo19
Myh10
Myo9b
Myl12a
Myl6
G
MDA-MB-231
Vehicle
MRCK Inhibitor
Invasive
Non-invasive
Percent of Total (%)
Vehicle
MRCKi
H
4T1
Vehicle
MRCK Inhibitor
Percent of Total (%)
Vehicle
MRCKi

Figure 2

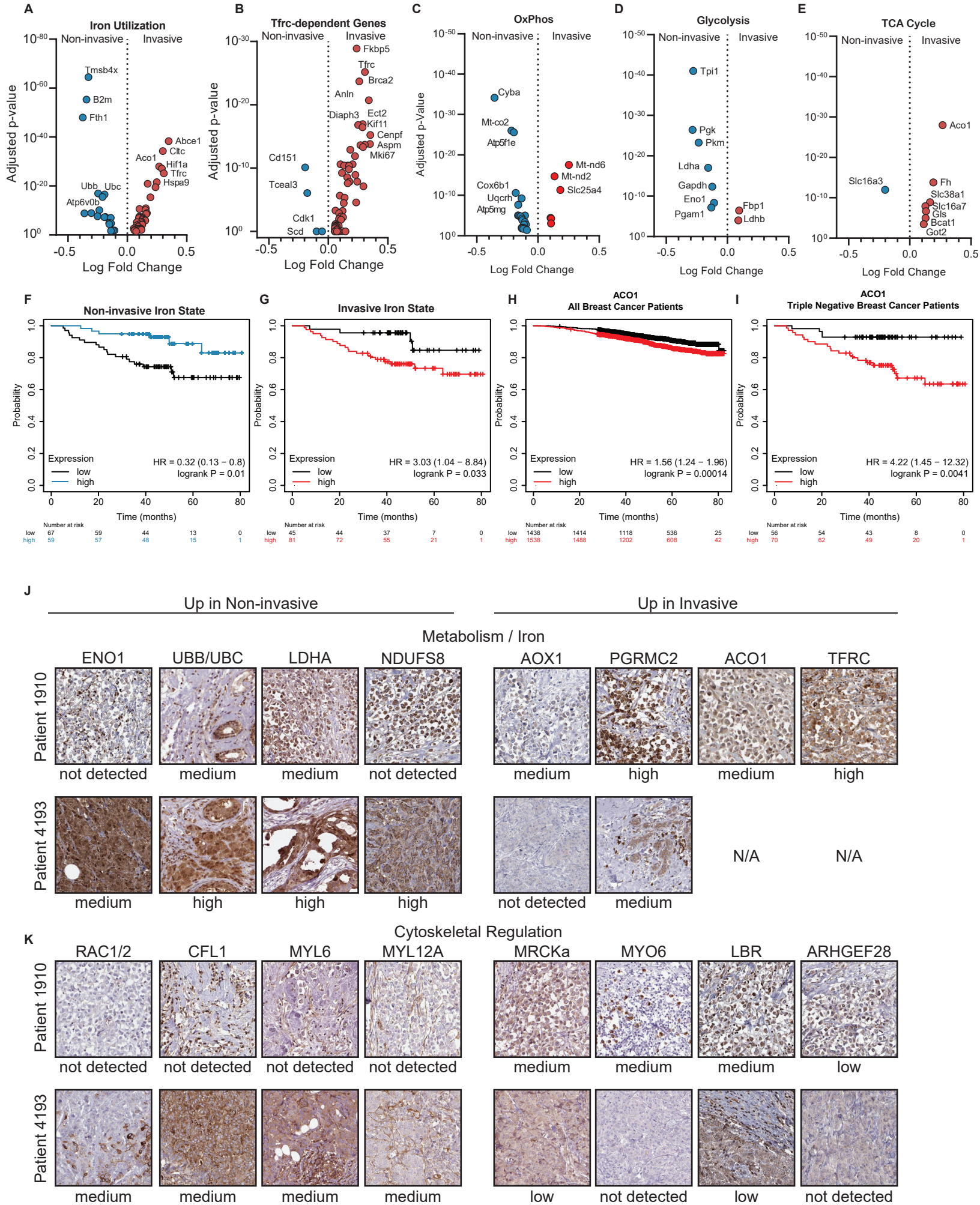
A
Iron Utilization
Non-invasive
Invasive
Adjusted p-value
Log Fold Change
Tmsb4x
B2m
Fth1
Abce1
Cltc
Aco1
Hif1a
Tfrc
Hspa9
Ubb
Ubc
Atp6v0b
B
Tfrc-dependent Genes
Fkbp5
Tfrc
Brca2
Anln
Diaph3
Ect2
Kif11
Cenpf
Aspm
Mki67
Cd151
Tceal3
Cdk1
Scd
C
OxPhos
Adjusted p-Value
Cyba
Mt-co2
Atp5f1e
Cox6b1
Uqcrh
Atp5mg
Mt-nd6
Mt-nd2
Slc25a4
D
Glycolysis
Tpi1
Pgk
Pkm
Ldha
Gapdh
Eno1
Pgam1
Fbp1
Ldhb
E
TCA Cycle
Aco1
Slc16a3
Fh
Slc38a1
Slc16a7
Gls
Bcat1
Got2
F
Non-invasive Iron State
Probability
Expression
low
high
HR = 0.32 (0.13 − 0.8)
logrank P = 0.01
Time (months)
Number at risk
low 67 59 44 13 0
high 59 57 48 15 1
G
Invasive Iron State
HR = 3.03 (1.04 − 8.84)
logrank P = 0.033
low 45 44 37 7 0
high 81 72 55 21 1
H
ACO1
All Breast Cancer Patients
HR = 1.56 (1.24 − 1.96)
logrank P = 0.00014
low 1438 1414 1118 536 25
high 1538 1488 1202 608 42
I
ACO1
Triple Negative Breast Cancer Patients
HR = 4.22 (1.45 − 12.32)
logrank P = 0.0041
low 56 54 43 8 0
high 70 62 49 20 1
J
Up in Non-invasive
Up in Invasive
Metabolism / Iron
ENO1
UBB/UBC
LDHA
NDUFS8
AOX1
PGRMC2
ACO1
TFRC
Patient 1910
not detected
medium
medium
not detected
medium
high
medium
high
Patient 4193
medium
high
high
high
not detected
medium
N/A
N/A
K
Cytoskeletal Regulation
RAC1/2
CFL1
MYL6
MYL12A
MRCKa
MYO6
LBR
ARHGEF28
Patient 1910
not detected
not detected
not detected
not detected
medium
medium
medium
low
Patient 4193
medium
medium
medium
medium
low
not detected
low
not detected

Figure 3

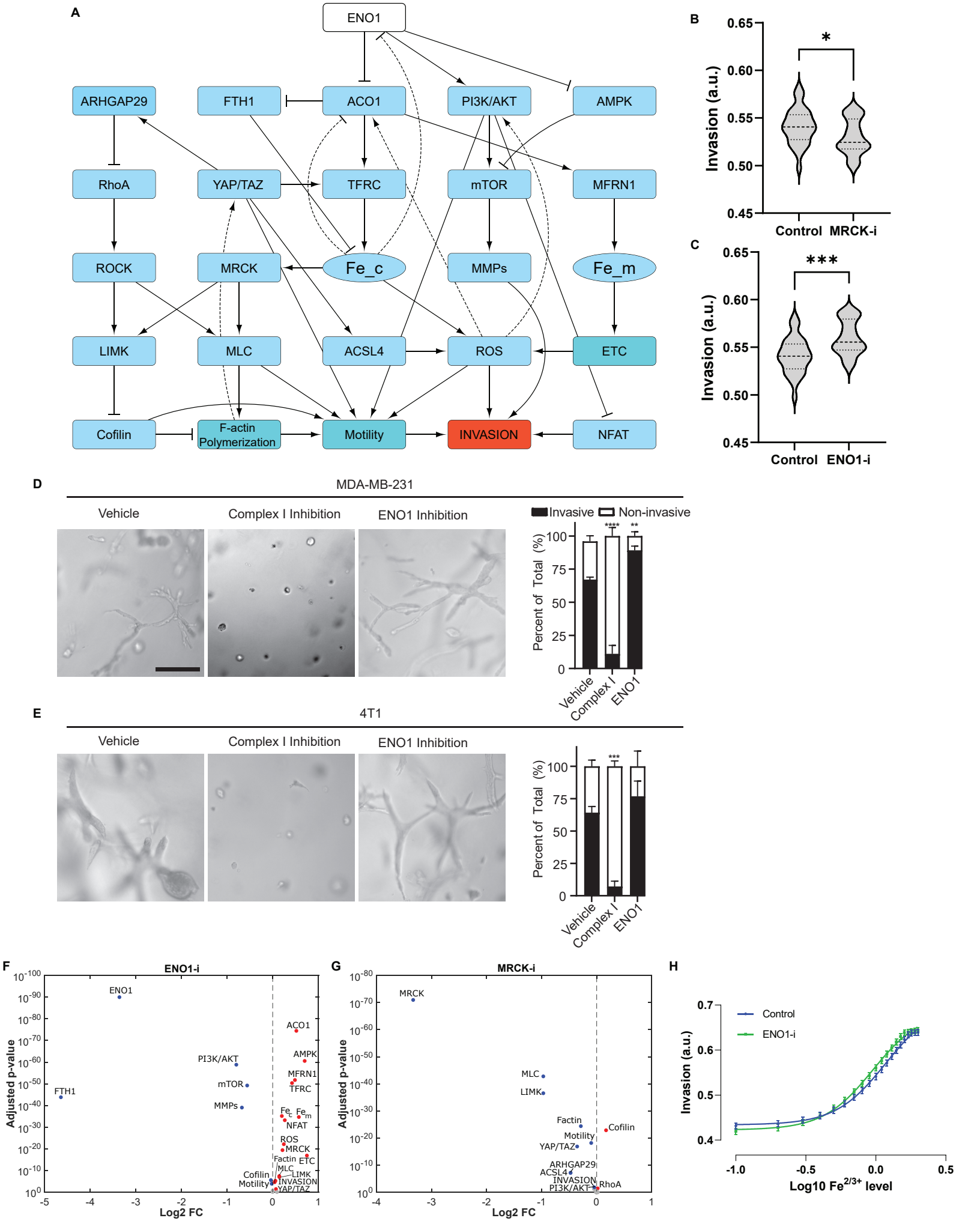
A
ENO1
ARHGAP29
FTH1
ACO1
PI3K/AKT
AMPK
RhoA
YAP/TAZ
TFRC
mTOR
MFRN1
ROCK
MRCK
Fe_c
MMPs
Fe_m
LIMK
MLC
ACSL4
ROS
ETC
Cofilin
F-actin Polymerization
Motility
INVASION
NFAT
B
Invasion (a.u.)
Control
MRCK-i
C
Invasion (a.u.)
Control
ENO1-i
D
MDA-MB-231
Vehicle
Complex I Inhibition
ENO1 Inhibition
Invasive
Non-invasive
Percent of Total (%)
Vehicle
Complex I
ENO1
E
4T1
Vehicle
Complex I Inhibition
ENO1 Inhibition
Percent of Total (%)
Vehicle
Complex I
ENO1
F
ENO1-i
Adjusted p-value
Log2 FC
G
MRCK-i
Adjusted p-value
Log2 FC
H
Control
ENO1-i
Invasion (a.u.)
Log10 Fe2/3+ level

Figure 4

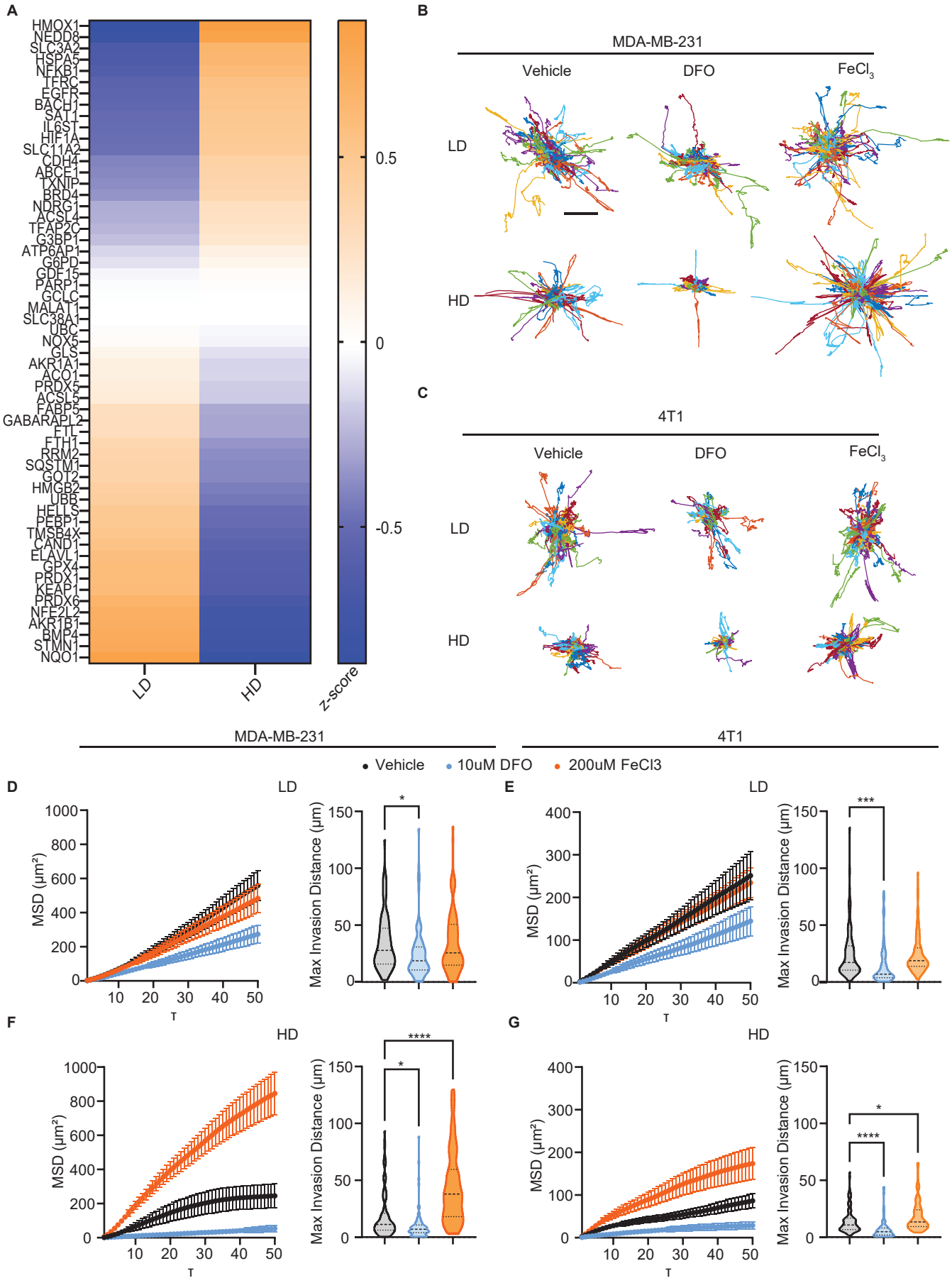
A
HMOX1
NEDD8
SLC3A2
HSPA5
NFKB1
TFRC
EGFR
BACH1
SAT1
IL6ST
HIF1A
SLC11A2
CDH4
ABCE1
TXNIP
BRD4
NDRG1
ACSL4
TFAP2C
G3BP1
ATP6AP1
G6PD
GDF15
PARP1
GCLC
MALAT1
SLC38A1
UBC
NOX5
GLS
AKR1A1
ACO1
PRDX5
ACSL5
FABP5
GABARAPL2
FTL
FTH1
RRM2
SQSTM1
GOT2
HMGB2
UBB
HELLS
PEBP1
TMSB4X
CAND1
ELAVL1
GPX4
PRDX1
KEAP1
PRDX6
NFE2L2
AKR1B1
BMP4
STMN1
NQO1
LD
HD
z-score
0.5
0
-0.5
B
MDA-MB-231
Vehicle
DFO
FeCl3
LD
HD
C
4T1
Vehicle
DFO
FeCl3
LD
HD
MDA-MB-231
4T1
Vehicle
10uM DFO
200uM FeCl3
D
LD
MSD (µm²)
T
Max Invasion Distance (µm)
*
E
LD
MSD (µm²)
T
Max Invasion Distance (µm)
***
F
HD
MSD (µm²)
T
Max Invasion Distance (µm)
*
****
G
HD
MSD (µm²)
T
Max Invasion Distance (µm)
*
****

Figure 5

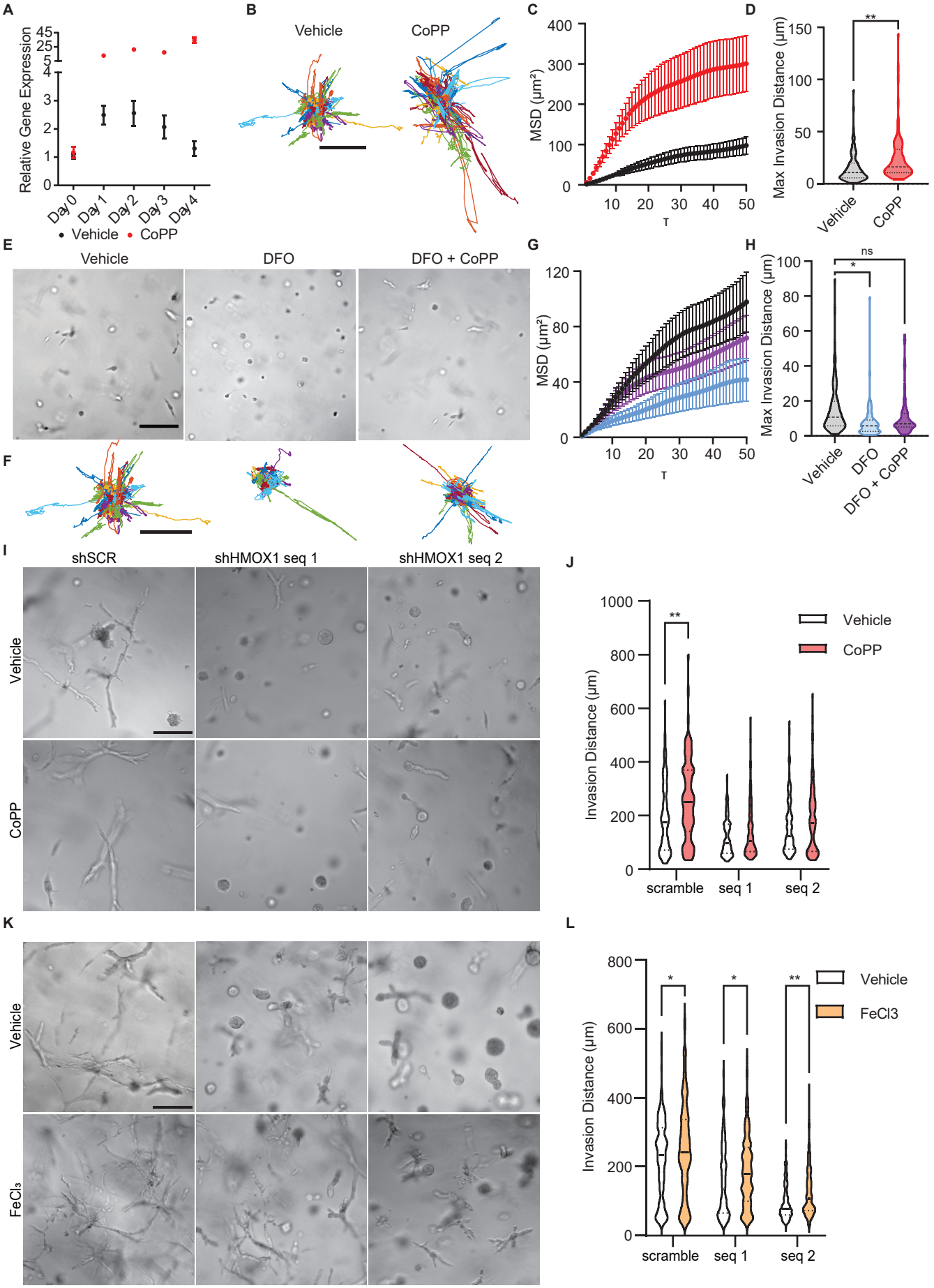
A
Relative Gene Expression
Day 0
Day 1
Day 2
Day 3
Day 4
Vehicle
CoPP
B
Vehicle
CoPP
C
MSD (µm²)
T
D
Max Invasion Distance (µm)
**
Vehicle
CoPP
E
Vehicle
DFO
DFO + CoPP
F
G
MSD (µm²)
T
H
Max Invasion Distance (µm)
ns
*
Vehicle
DFO
DFO + CoPP
I
shSCR
shHMOX1 seq 1
shHMOX1 seq 2
Vehicle
CoPP
J
Invasion Distance (µm)
**
Vehicle
CoPP
scramble
seq 1
seq 2
K
Vehicle
FeCl₃
L
Invasion Distance (µm)
*
*
**
Vehicle
FeCl3
scramble
seq 1
seq 2

Figure S1

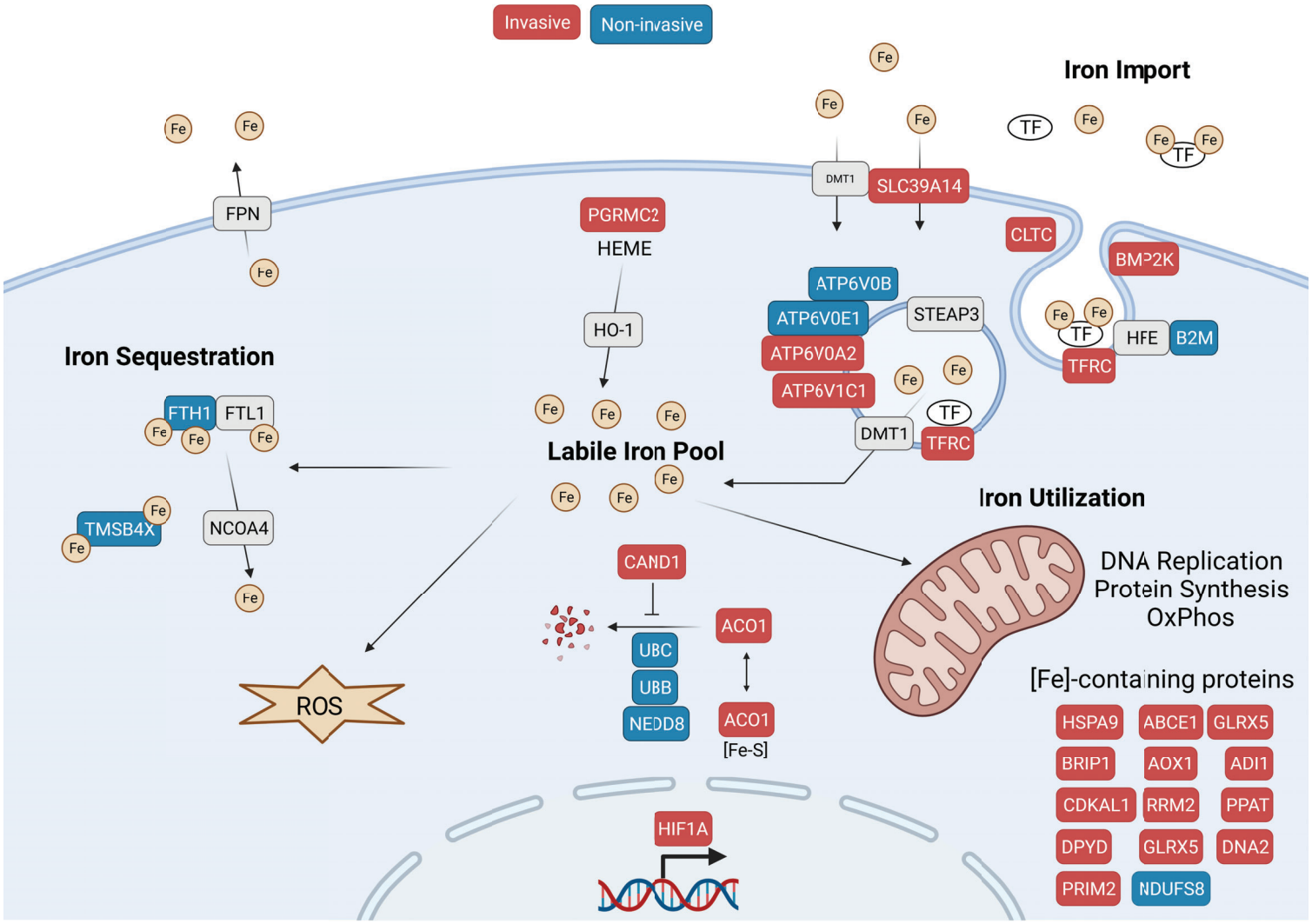
Invasive
Non-invasive
Iron Import
Fe
TF
DMT1
SLC39A14
CLTC
BMP2K
HFE
B2M
TFRC
FPN
PGRMC2
HEME
HO-1
ATP6V0B
ATP6V0E1
ATP6V0A2
ATP6V1C1
STEAP3
Iron Sequestration
FTH1
FTL1
TMSB4X
NCOA4
Labile Iron Pool
Iron Utilization
DNA Replication
Protein Synthesis
OxPhos
[Fe]-containing proteins
HSPA9
ABCE1
GLRX5
BRIP1
AOX1
ADI1
CDKAL1
RRM2
PPAT
DPYD
GLRX5
DNA2
PRIM2
NDUFS8
CAND1
ACO1
UBC
UBB
NEDD8
ACO1
[Fe-S]
ROS
HIF1A

Figure S2

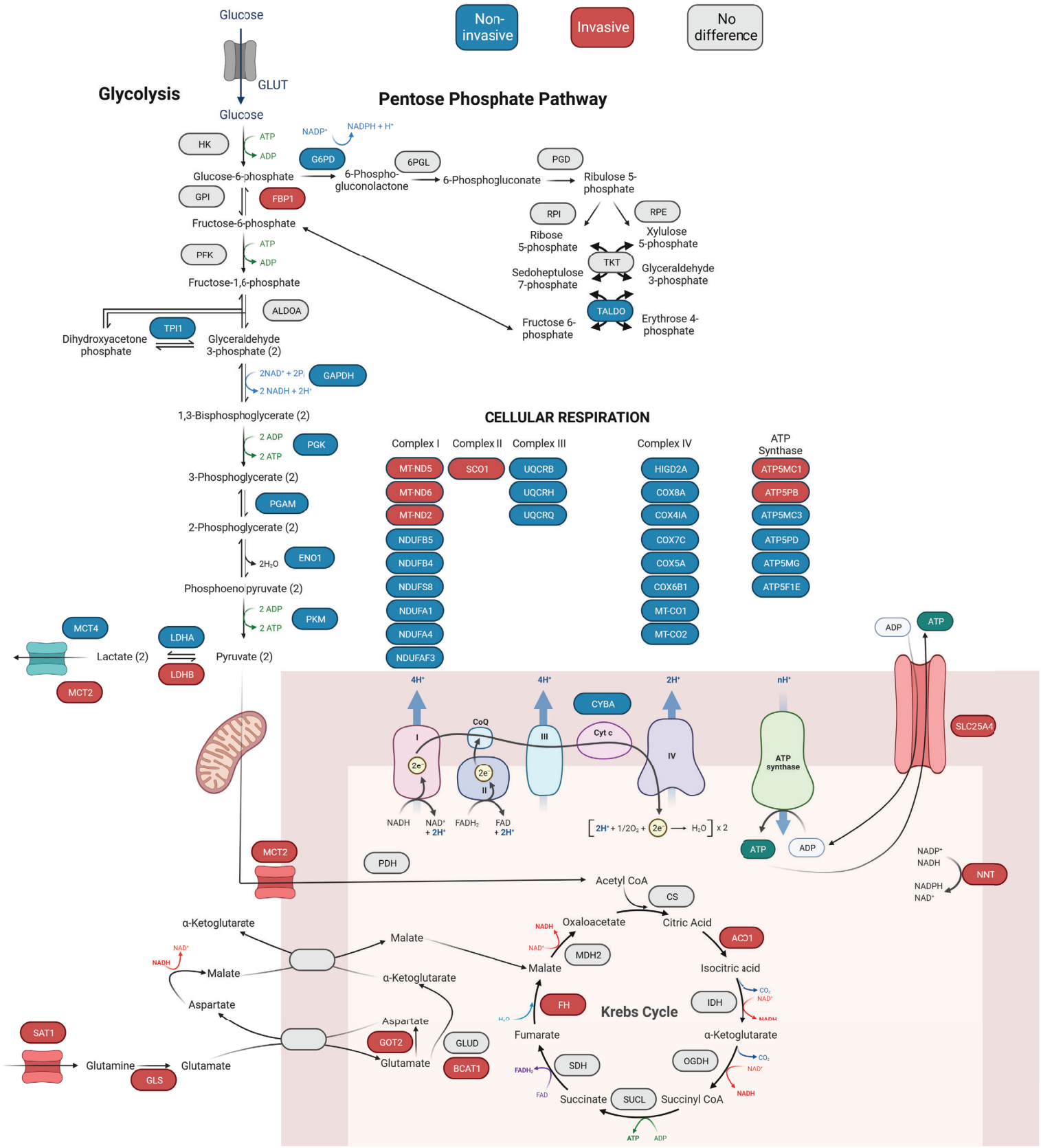
Non-invasive
Invasive
No difference
Glucose
GLUT
Glycolysis
Glucose
HK
ATP
ADP
Glucose-6-phosphate
GPI
FBP1
Fructose-6-phosphate
PFK
ATP
ADP
Fructose-1,6-phosphate
ALDOA
TPI1
Dihydroxyacetone phosphate
Glyceraldehyde 3-phosphate (2)
2NAD⁺ + 2Pᵢ
2 NADH + 2H⁺
GAPDH
1,3-Bisphosphoglycerate (2)
2 ADP
2 ATP
PGK
3-Phosphoglycerate (2)
PGAM
2-Phosphoglycerate (2)
2H₂O
ENO1
Phosphoenolpyruvate (2)
2 ADP
2 ATP
PKM
Pyruvate (2)
LDHA
LDHB
Lactate (2)
MCT4
MCT2
Pentose Phosphate Pathway
NADP⁺
NADPH + H⁺
G6PD
6-Phospho-gluconolactone
6PGL
6-Phosphogluconate
PGD
Ribulose 5-phosphate
RPI
RPE
Ribose 5-phosphate
Xylulose 5-phosphate
TKT
Sedoheptulose 7-phosphate
Glyceraldehyde 3-phosphate
TALDO
Fructose 6-phosphate
Erythrose 4-phosphate
CELLULAR RESPIRATION
Complex I
Complex II
Complex III
Complex IV
ATP Synthase
MT-ND5
MT-ND6
MT-ND2
NDUFB5
NDUFB4
NDUFS8
NDUFA1
NDUFA4
NDUFAF3
SCO1
UQCRB
UQCRH
UQCRQ
HIGD2A
COX8A
COX4IA
COX7C
COX5A
COX6B1
MT-CO1
MT-CO2
ATP5MC1
ATP5PB
ATP5MC3
ATP5PD
ATP5MG
ATP5F1E
4H⁺
4H⁺
2H⁺
nH⁺
CoQ
CYBA
Cyt c
ATP synthase
NADH
NAD⁺ + 2H⁺
FADH₂
FAD + 2H⁺
[2H⁺ + 1/2O₂ + 2e⁻ → H₂O] x 2
ADP
ATP
SLC25A4
NADP⁺
NADH
NADPH
NAD⁺
NNT
MCT2
PDH
Acetyl CoA
CS
Citric Acid
ACO1
Isocitric acid
IDH
α-Ketoglutarate
OGDH
Succinyl CoA
SUCL
Succinate
SDH
FADH₂
FAD
Fumarate
FH
Malate
MDH2
Oxaloacetate
Krebs Cycle
α-Ketoglutarate
Malate
Malate
α-Ketoglutarate
Aspartate
Aspartate
GOT2
Glutamate
GLUD
BCAT1
Glutamine
GLS
Glutamate
SAT1

Figure S3

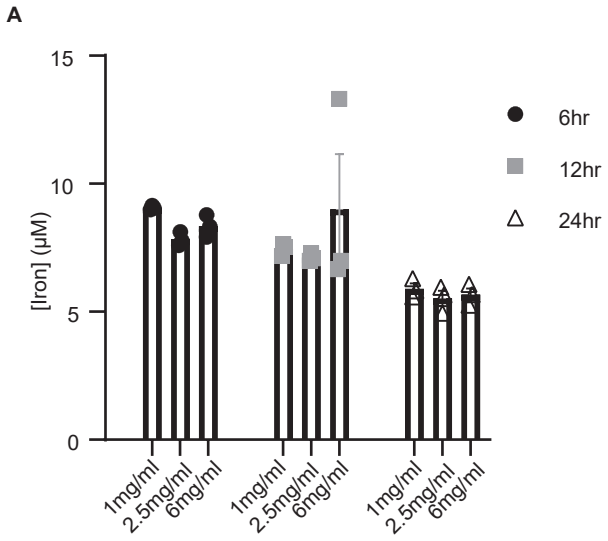
A
15
10
5
0
[Iron] (µM)
6hr
12hr
24hr
1mg/ml
2.5mg/ml
6mg/ml
1mg/ml
2.5mg/ml
6mg/ml
1mg/ml
2.5mg/ml
6mg/ml
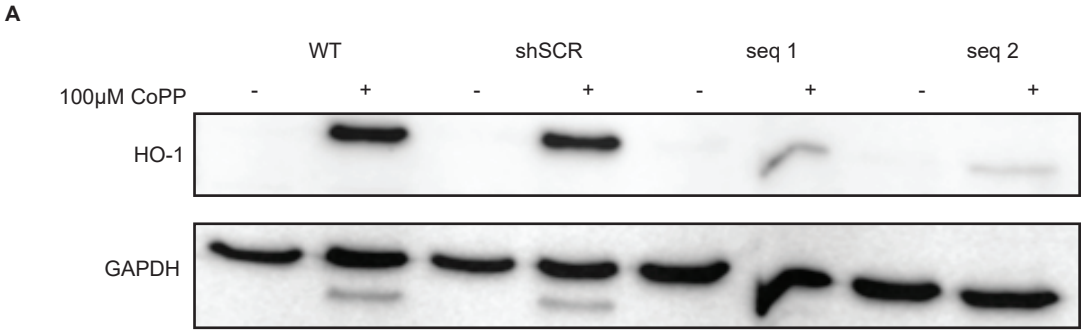
Figure S4